



## 3D SPARKLING trajectories for high-resolution T2\*-weighted Magnetic Resonance imaging

Carole Lazarus, Pierre Weiss, Loubna El Gueddari, Franck Mauconduit,  
Alexandre Vignaud, Philippe Ciuciu

### ► To cite this version:

Carole Lazarus, Pierre Weiss, Loubna El Gueddari, Franck Mauconduit, Alexandre Vignaud, et al..  
3D SPARKLING trajectories for high-resolution T2\*-weighted Magnetic Resonance imaging. 2019.  
hal-02067080

**HAL Id: hal-02067080**

**<https://inria.hal.science/hal-02067080>**

Preprint submitted on 14 Mar 2019

**HAL** is a multi-disciplinary open access archive for the deposit and dissemination of scientific research documents, whether they are published or not. The documents may come from teaching and research institutions in France or abroad, or from public or private research centers.

L'archive ouverte pluridisciplinaire **HAL**, est destinée au dépôt et à la diffusion de documents scientifiques de niveau recherche, publiés ou non, émanant des établissements d'enseignement et de recherche français ou étrangers, des laboratoires publics ou privés.

# 3D SPARKLING trajectories for high-resolution T2\*-weighted Magnetic Resonance imaging

Carole Lazarus, Pierre Weiss, Loubna El Gueddari, Franck Mauconduit, Alexandre Vignaud  
and Philippe Ciuciu *Senior Member*

**Abstract**—We have recently proposed a new optimization algorithm called SPARKLING (Spreading Projection Algorithm for Rapid K-space samPLING) to design efficient Compressive Sampling patterns for Magnetic Resonance Imaging. This method has a few advantages over standard trajectories such as radial lines or spirals: i) it allows to sample the k-space along any arbitrary density while the other two are restricted to radial densities and ii) it achieves a higher image quality for a given readout time. Here, we introduce an extension of the SPARKLING method for 3D imaging that allows to achieve an isotropic resolution of 600  $\mu\text{m}$  in just 45 seconds, compared to a scan duration of 14 min 31 s using 4-fold accelerated parallel imaging, for T2\*-weighted *ex vivo* brain imaging at 7 Tesla over a field-of-view of  $200 \times 200 \times 140 \text{ mm}^3$ .

**Index Terms**—3D MRI, optimization, non-Cartesian, compressed sensing, acceleration, SWI.

## I. INTRODUCTION

To reduce scan time in MRI, sampling along non-Cartesian trajectories may prove to be advantageous. An efficient use of the MR gradient hardware can indeed enable rapid coverage of the k-space. When combined with compressed sensing, the use of undersampled non-Cartesian trajectories can allow further reduction in the acquisition time [1]. In this context, it was shown that k-space trajectories should perform a variable density sampling for best performance [2]–[4].

Three-dimensional (3D) compressed acquisitions are usually performed with 3D radial trajectories [5] or Poisson Disk lines [6]. The former observes a fully 3D variable density while the latter performs a 2D Poisson disk variable density orthogonally to the readout lines. Let us mention a few other fully 3D sampling strategies based on analytical expression such as 3D cones [7], twisted projections (TPI) [8] and hybrid radial-cones [9]. A few works attempted to use optimization principles to design 3D trajectories [10]–[12], but did not include clear sampling criteria.

Recently, we introduced a new optimization-driven method named SPARKLING (Spreading Projection Algorithm for Rapid K-space samPLING) [13]–[15]. This algorithm inspired from stippling techniques automatically generates optimized sampling patterns compatible with MR hardware constraints on maximum gradient amplitude and slew rate. These non-Cartesian sampling curves are designed to comply with key criteria for optimal sampling: a controlled distribution of samples

(e.g., a variable density) and a locally uniform k-space coverage. The SPARKLING strategy was used for 2D  $T_2^*$  high-resolution *in vivo* brain imaging and was shown to yield higher image quality compared to standard geometrical patterns such as radial or spiral trajectories, while allowing high acceleration factors up to 20 compared to standard Cartesian scans [15]. The proposed method may hence improve the trade-off between sampling efficiency and robustness to artifacts.

In this paper, we explore how the principles of the SPARKLING method can be extended to design 3D trajectories, expecting to benefit from higher signal-to-noise ratio (SNR) conditions. We begin by exploring the use of stack of 2D trajectories (such as stack of stars [16], [17], stack of spirals [7], [18] or stack of EPI [19]). Then, we turn to fully 3D trajectories, which have the potential to respect a truly 3D variable density necessary for an optimal use of compressed sensing in 3D [20], [21].

We perform 3D prospective *ex vivo* MR acquisitions and compare our method against several 3D sampling strategies including Cartesian, 3D radial [5] and Poisson Disk lines [6]. Our experiments involve prospective high resolution *ex vivo*  $T_2^*$  acquisitions performed at 7 Tesla.

## II. OPTIMIZATION-DRIVEN DESIGN OF SAMPLING PATTERNS IN MRI

### A. 2D K-space trajectory

A k-space trajectory is usually composed of several segments  $\mathbf{k}(t) = (k_x(t), k_y(t))$ , also referred to as shots, which are controlled by magnetic field gradients  $\mathbf{G}(t) = (G_x(t), G_y(t))$  as follows:

$$\mathbf{k}(t) = \frac{\gamma}{2\pi} \int_0^t \mathbf{G}(\tau) d\tau, \quad (1)$$

where  $\gamma$  denotes the gyro-magnetic ratio. Hardware constraints on the maximum gradient amplitude ( $G_{max}$ ) and slew rate ( $S_{max}$ ) induce limitations in trajectory speed and acceleration. These limits can be expressed as inequality range constraints on each of the time points of the discrete waveform  $\mathbf{k} = (\mathbf{k}[i])_{1 \leq i \leq p}$  where  $\mathbf{k}[i] = (k_x[i], k_y[i])$ ,  $\forall 1 \leq i \leq p$  and  $p$  is the number of gradient time-steps. Typically, rotation invariant speed and acceleration constraint can be expressed as follows<sup>1</sup>

<sup>1</sup>In [22], we have also dealt with the case of rotation variant constraints where the  $\ell_\infty$ -norm replaces the mixed  $\ell_{2,\infty}$ -norm here.

$$\|\dot{\mathbf{k}}\|_{2,\infty} < \frac{\gamma}{2\pi} G_{\max} \quad (2a) \quad \|\dot{\mathbf{k}}\|_{2,\infty} < \frac{\gamma}{2\pi} S_{\max} \quad (2b)$$

where  $\|\mathbf{c}\|_{2,\infty} = \sup_{1 \leq i \leq p} (|\mathbf{c}_x[i]|^2 + |\mathbf{c}_y[i]|^2)^{1/2}$  and

$$\begin{cases} \dot{\mathbf{k}}[i] &= \frac{\mathbf{k}[i] - \mathbf{k}[i-1]}{dt}, \\ \ddot{\mathbf{k}}[i] &= \frac{\mathbf{k}[i+1] - 2\mathbf{k}[i] + \mathbf{k}[i-1]}{dt^2} \end{cases} \quad (3)$$

Here  $dt$  is the gradient raster time and in practice it may be different from the dwell time  $\Delta t$ . However, in what follows, we set  $\Delta t = \delta t$ .

Following [15], we let  $\mathcal{Q}_p$  denote the set of  $k$ -space discrete curves respecting the aforementioned constraints (2a)-(2b). Note that  $\mathcal{Q}_p$  can be completed to account for any affine constraint such as the specification of  $\mathbf{k}$  at the echo-time (TE):  $\mathbf{k}[TE] = 0$ . In the context of multi-shot acquisitions, these constraints apply to every shot independently. We now briefly remind the minimization problem we solve in the SPARKLING algorithm framework [14], [15] to point out the challenges raised in 3D imaging afterwards.

### B. The SPARKLING algorithm

Our objective is to minimize a  $\ell_2$  distance between a target density  $\rho : \mathbb{R}^3 \rightarrow \mathbb{R}$  and a sampling trajectory  $\mathbf{k}$  under the aforementioned constraints :

$$\min_{\mathbf{k} \in \mathcal{Q}_p} \text{dist}(\rho, \nu(\mathbf{k})) = \min_{\mathbf{k} \in \mathcal{Q}_p} \frac{1}{2} \|h \star (\nu(\mathbf{k}) - \rho)\|_2^2 \quad (4)$$

where  $h$  is a continuous interpolation kernel, symbol  $\star$  denotes the convolution operator,  $\nu(\mathbf{k})$  is the discrete measure supported by the curve  $\mathbf{k}$  (see [13] for the definition of  $\nu$  and more details). The distance in Eq. (4) can be conveniently rewritten by expanding the  $\ell_2$ -norm into:

$$\min_{\mathbf{k} \in \mathcal{Q}_p} \underbrace{\frac{1}{p} \sum_{i=1}^p \int_{\Omega} H(x - \mathbf{k}[i]) \rho(x) dx}_{F_a(\mathbf{k})} - \underbrace{\frac{1}{2p^2} \sum_{1 \leq i, j \leq p} H(\mathbf{k}[i] - \mathbf{k}[j])}_{F_r(\mathbf{k})} \quad (5)$$

where the Fourier transform  $\hat{H}$  of  $H$  is equal to  $|\hat{h}|^2$ . In our experiments, we selected the Euclidean distance  $H(x) = \|x\|_2$  [14], [23]. Problem (5) can be interpreted as the minimization of a potential energy  $F = F_a - F_r$  containing an attractive term  $F_a$  (bringing together samples according to the target density  $\rho$ ) and a repulsive term  $F_r$  (avoiding the formation of gaps and clusters of samples). After calculation of the derivatives of these two terms, this non-convex cost function can be minimized by a projected gradient descent of the type  $\mathbf{k}_{t+1} = \Pi_{\mathcal{Q}_p}(\mathbf{k}_t - \beta_t \nabla F(\mathbf{k}_t))$ , which alternates between a non-convex distance minimization part and a projection onto the convex MR constraints  $\mathcal{Q}_p$ . We refer to [24] for more details on the computation of the gradient  $\nabla F$  and to [22] for details about the projection on  $\mathcal{Q}_p$ .

### C. Stack-of-SPARKLING

A first strategy to perform 3D imaging with the SPARKLING method is to use 2D SPARKLING trajectories and stack them along the partition direction denoted here as  $z$ . This approach is illustrated in Fig. 1a for a stack of 10 identical SPARKLING trajectories, which will be referred to as *regular stack-of-SPARKLING* or *regular SOS*. To respect the Nyquist criterion along the partition direction, the  $N_z$  stacks should be spaced by a  $\text{FOV}_z^{-1}$ -distance until reaching the desired maximum spatial frequency. In the situation of a regular SOS, no variable density is performed along the partition direction.

More interestingly, to subsample the partition direction and obtain a fully 3D variable density, the target density may be changed according to the plane's altitude  $k_z$ . Given a 3D density  $\rho \in \mathbb{R}^{N \times N \times N_z}$ , a 2D SPARKLING trajectory at altitude  $k_z$  will be generated using the density  $\rho_{2D}(k_z) = \frac{\rho(:, :, k_z)}{\int \rho(:, :, k_z)}$ . In addition, once the number of shots in the central stack  $n(0)$  is chosen, the mass of each plane can be adapted to the plane density by reducing the number of shots per altitude, as  $k_z$  increases:

$$n(k_z) = n(0) \frac{\int \rho(:, :, k_z)}{\int \rho(:, :, 0)}, \quad (6)$$

where  $n(k_z)$  is the number of shots in the plane of altitude  $k_z$ . Fig. 1b shows such a stack for an isotropic density (defined on a 3D ball) for 10 SPARKLING trajectories. This design will be referred to as *z-variable-density stack-of-SPARKLING* or *z- $\nu$ d SOS*. Further acceleration may be reached by subsampling the number of planes and using parallel imaging along this direction.

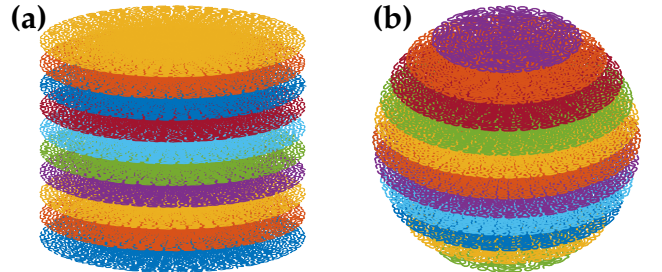


Fig. 1. Stack of 10 identical SPARKLING trajectories filling a cylinder (a) and stack of 11 variable SPARKLING trajectories filling a 3D ball (b). (Colors are just for visualization purposes).

### D. Fully 3D SPARKLING

To perform a fully 3D sampling of the  $k$ -space, it is also possible to extend the SPARKLING algorithm presented in [14] to three dimensions. Such segmented sampling scheme is composed of non-Cartesian curves spanning all 3  $k$ -space directions, filling a ball of radius  $k_{\max}$ , where  $k_{\max}$  is the maximum radial extent in the 3D  $k$ -space.

1) *Algorithmic extension*: The SPARKLING algorithm's bottleneck lies in the calculation of the gradient of the repulsive term  $F_r$  between the samples in Eq. (5), where

there is a summation over all the samples. In 3D, this summation was calculated directly using a two-level nested loop, which gives a complexity of  $O(p^2)$ , where  $p$  is the number of particles in  $\mathbf{k}$ . For high resolution imaging, we need of the order of  $p = 10^7$  particles, making this method irrelevant. The brute-force method could be accelerated using 3D techniques used for the simulation of particles (e.g. NFFT or fast multipole methods), but would require complex numerical libraries. The brute-force method could be accelerated using techniques used for the simulation of particles (e.g. NFFT or fast multipolar methods), but would require the use of complex numerical libraries. In this work, since our objective is to target *radial densities*, which ensure rotation invariant reconstruction results, we propose an alternative technique described below.

2) *Using a regular sphere tessellation to accelerate the process:* The idea is to generate each shot independently from the others, by truncating the target density into  $n_s$  volumetric sectors filling the considered  $\mathbf{k}$ -space, where  $n_s$  is the desired total number of shots. To further accelerate the process, we can reduce the number of SPARKLING-processed shots by using a semi-regular partition of the sphere. We used an equal-area tessellation which divides the sphere into regions of equal area [25], as is displayed in Fig. 2a for  $n_s = 100$ . The property of equal area is important insofar as it ensures that all 3D sectors have equal mass in the case of a radial density. Furthermore, for a constant elevation angle (highlighted in blue on Fig. 2a-b), all tiles are exactly identical and the associated trajectory can be obtained from another one using a simple rotation. Hence, only a small fraction of the desired total number of shots needs to be generated, namely one per latitude. This leads to a reduction in computation time by a factor 20 to 30. Using this strategy, the typical computational time to generate 1000 shots for a matrix size of  $N = 256$  is about 20 minutes on a Intel Xeon(R) CPU at 2.20 GHz with 40 cores.

In the case of center-out shots, a 3D sector is created by connecting the four summits of a spherical tile to the origin of the  $\mathbf{k}$ -space. If symmetric shots for which the echo time TE is at the middle of the segment, are desired, the latter sector constitutes one half of total symmetric sector and the other half is obtained by rotating the latter about the origin, as displayed in Fig. 2b. To avoid discontinuity between the two halves, the sector is slightly thickened near the origin. For example, with this strategy, only 7 symmetric shots need to be produced by the SPARKLING algorithm for  $n_s = 100$ . Fig. 2b shows one SPARKLING shot, corresponding to the highlighted sector for a radially decaying density and for a matrix size of  $128 \times 128 \times 128$ ,  $k_{max} = 320 \text{ m}^{-1}$ ,  $G_{max} = 40 \text{ mT/m}$  and  $S_{max} = 200 \text{ T/m/s}$ . This shot is then rotated to fill the regions of equal elevation angle, as depicted in Fig. 2c. The process is repeated for all latitudes, generating the fully 3D SPARKLING trajectory shown in Fig. 2d.

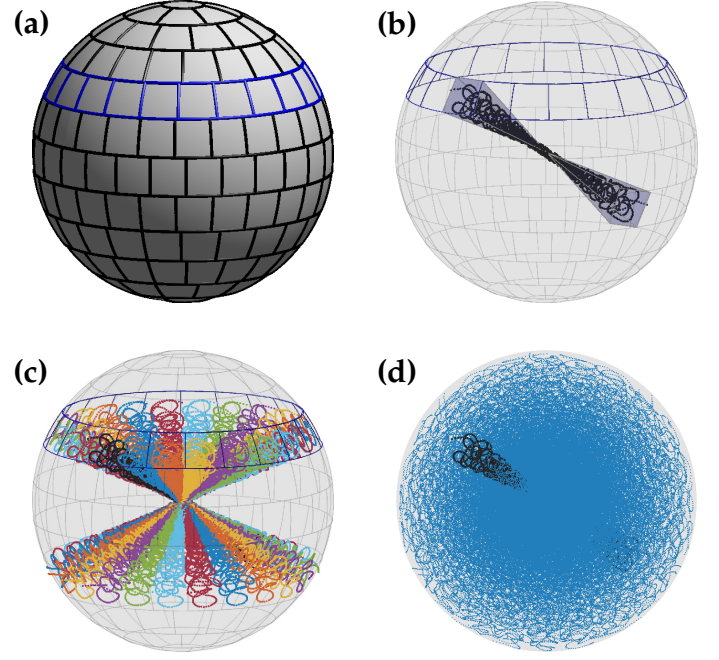


Fig. 2. 3D SPARKLING process. (a): Partition of the sphere into 100 regions of equal area. Regions along a constant elevation angle were highlighted in blue: they are identical up to a rotation. (b): One 3D density sector containing a SPARKLING shot. (c): The SPARKLING shot is then rotated along the considered latitude. (d): the whole fully 3D SPARKLING trajectory. Parameters are:  $N = 128$ ,  $k_{max} = 320 \text{ m}^{-1}$ , 100 symmetric shots and 7 shots to generate (6 latitudes + 1 conic cap).

#### E. Selection of the target density

In view of the long computation time required for reconstructing 3D MR images, the target density was retrospectively selected among a set of 6 radially decaying densities. We consider here a radial isotropic density of the form  $\nu : \mathbf{k} \mapsto \frac{1}{|\mathbf{k}|^d}$ , which decays as an inverse polynomial. The singularity at the origin is truncated by the method introduced in [15] allowing to create a circular plateau at Shannon's rate at the origin. Two parameters of the density were varied here: the decay rate  $d \in \{2, 3\}$  and the plateau threshold  $\tau \in \{0.5, 0.75, 1\}$ . Fig. 3 shows the 6 tested densities for  $N = 320$ . To rank the different densities, evenly

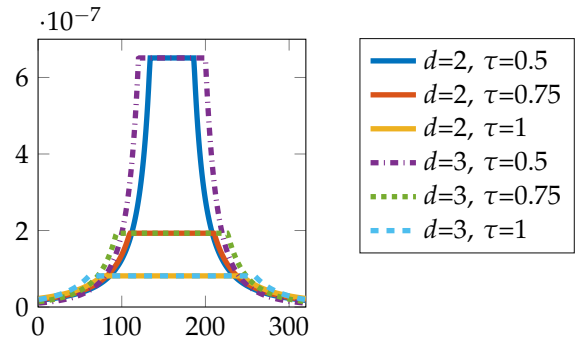


Fig. 3. The 6 tested densities  $\nu$  for  $N = 320$ .

spaced samples were drawn along each density by using Lloyd's algorithm, also known as Voronoi iteration [26].



Lloyd's method allows to quickly produce a distribution of points with blue noise characteristics, i.e. to produce a locally uniform coverage. The initial positions of the  $p$  samples were determined with an i.i.d. drawing along the considered density. Then, Lloyd's algorithm was applied using 10 cycles. Once the 3D samples are produced for  $p = 10^6$  and all densities, the corresponding retrospectively generated Fourier data of a 3D baboon brain image are reconstructed using nonlinear 3D reconstructions (details about image reconstruction are provided in Section IV). The density which gives the best image quality both visually and in terms of pSNR is selected and will be used as a 3D target density for the SPARKLING trajectories. For instance, in the case of  $N = 320$ , we selected the density with  $d = 3$  and  $\tau = 0.75$ .

### III. PROSPECTIVE 3D SPARKLING ACQUISITION

3D acquisitions were performed on a 7 Tesla MR scanner (Siemens Healthineers, Erlangen, Germany) with a 1Tx/32Rx head coil (Nova Medical, Wilmington, MA, USA). The maximum gradient amplitude and slew rate for this system were 40 mT/m and 200 T/m/s, respectively. A 3D Gradient Recalled Echo (GRE) sequence was used. The imaging parameters were: TR=40 ms, TE=20 ms, FA=15°,  $T_{obs}$ =15.36 ms and BW=200 kHz.

For different setups, prospective acquisitions were performed on an *ex vivo* baboon brain conserved in a fluorinert solution. All animal studies were conducted in accordance with the European convention for animal care and the NIHs Guide for the Care and Use of Laboratory Animals. First, for an isotropic resolution of 0.6 mm, the three proposed SPARKLING trajectories were compared: regular SOS, z-vd SOS and fully 3D SPARKLING. As reference, we also performed a standard Cartesian iPAT acquisition with GRAPPA reconstruction available on the scanner (Siemens product sequence) either for iPAT 4 (4x1 and 24 reference lines), iPAT 2 (24 reference lines) with Partial Fourier 6/8 (phase and encode). Furthermore, the 3D SPARKLING strategy was compared to other 3D trajectories used in compressed sensing MRI. First, the 3D Poisson disk strategy introduced by Lustig et al [6] was considered. This method, which will be referred to as *PD-lines*, consists in acquiring along the partition direction cross-sections of 2D Poisson disk samples with a deterministic sampling of the k-space center (see Fig. 4c). The size of the deterministically sampled region and the radially decaying rate of the density outside this region were selected using a grid-search on retrospectively subsampled reconstructions of a brain phantom image. Second, 3D radial trajectories were also acquired for comparison [5] (see Fig. 4b). Since [15] already investigated the performance of 2D SPARKLING against radial and variable-density spiral trajectories, we did not investigate here the stack-of-stars nor the stack-of-spirals. We expect the relative performance of 2D sampling patterns to remain the same when they are stacked into 3D trajectories.

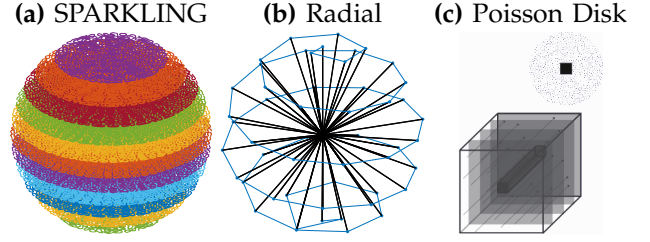


Fig. 4. We compare three 3D sampling schemes: the proposed z-variable density SOS, the 3D radial-trajectories [5] and the so-called Poisson Disk approach proposed in [1], [6].

Finally, a high resolution of 0.3 mm in the axial plane with a slice thickness of 1.5 mm was performed, similar to the protocols presented in the literature [27]–[29]. Table I summarizes the studied protocols and the different acceleration setups. The acceleration factor  $AF$  is calculated as a function of the fully-sampled Cartesian scan; it is given as the ratio of the number of lines in the reference scan over the number of shots in the accelerated scan (see its formula in Table I).

### IV. 3D MR IMAGE RECONSTRUCTION

Images were reconstructed using a 3D extension of a self-calibrating reconstruction algorithm [30] that deals with non-Cartesian k-space data collected over a multichannel phased array and that promotes sparsity in the wavelet transform domain. The original code was implemented in Matlab and already used in [15] but an open source code is now available in Python in the PySAP software<sup>2</sup> both for 2D and 3D imaging. To speed up the reconstruction process in 3D imaging, the NFFT [31] was replaced with the GPU nufft<sup>3</sup>. Also, for the sake of efficiency, all 3D MR images were reconstructed using a Symmlet 8 orthogonal wavelet transform, an  $\ell_1$ -sparsity promoting regularization. A FISTA algorithm was used to minimize the overall convex but nonsmooth objective function. A single regularization parameter was grid searched over the range  $(10^{-7}, 10^{-2})$  to optimize the structural similarity (SSIM) as a measure of image quality. Yet, the reconstruction time remained quite long, especially for treating 32 channel-receiver coil data, reaching about 4 hours for  $N = 256$  and 400 iterations, including the calculation of the Lipschitz constant, with a NVIDIA GPU card GM204GL Quadro M4000 (1664 cores, global memory 8 GB).

## V. RESULTS

### A. Comparison of the different SPARKLING strategies

First, different 3D SPARKLING strategies were compared for an isotropic resolution of 0.6 mm. Regular

<sup>2</sup><https://github.com/CEA-COSMIC/pysap>

<sup>3</sup>The Matlab API we used was developed by A. Schwarzl and F. Knoll, <http://cai2r.net/resources/software/gpunufft-open-source-gpu-library-3d-gridding-direct-matlab-interface>, whereas the one in Python was developed by J-M. Lin and is available in pynufft [32], cf <https://github.com/jyhmiinlin/pynufft>.

TABLE I  
ACQUISITION PARAMETERS USED FOR 3D K-SPACE TRAJECTORY DESIGN.

FOV (mm <sup>3</sup> )	Matrix size	Resolution (mm)	Number of shots $n_s$	Total scan time (TA)	$AF = \frac{N \times N_z}{n_s}$
$200 \times 200 \times 140$	$320 \times 320 \times 224$	$0.6 \times 0.6 \times 0.6$	4010	2 min 40 s	18
			2050	1 min 22 s	35
			1040	45 s	69
$200 \times 200 \times 140$	$640 \times 640 \times 96$	$0.3 \times 0.3 \times 1.5$	4085	2 min 43 s	15
			2090	1 min 24 s	30

SOS, z-variable SOS and fully 3D SPARKLING trajectories were acquired for two different acquisition times: 2 min 40 s and 1 min 22 s, see Table I for details on acquisition parameters. A Cartesian iPAT 4 scan (TA = 14 min 31 s) was also collected and will be considered as the reference image quality. Results in transversal, coronal, sagittal planes and a magnified central region of the axial slice are shown in Fig. 5 for a SPARKLING acquisition time of 2 min 40 s. Each column corresponds to a different sampling method.

For both acceleration factors of 18 and 35, the image quality is well preserved especially in the dendritic arborization in the cerebellum, which is visible in the sagittal plane. One may notice that the fully 3D SPARKLING results are not as good as those obtained using the SOS strategy, as they appear more blurry. Regular and z-variable SOS yield similar image quality as is corroborated by the SSIM scores measured on an axial slice taking the iPAT 4 image as a reference. A similar trend was observed for the shorter acquisition of 1 min 22 s (data not shown).

#### B. Comparison with existing sampling trajectories

3D SPARKLING trajectories were also compared to 3D radial and Poisson disk sampling strategies for a large acceleration factor of 69, corresponding to an acquisition time of 45 s. Here, a z-variable-density stack-of-SPARKLING was used for SPARKLING acquisitions since it yielded better image quality among the previously tested 3D SPARKLING strategies and has the advantage of supporting high acceleration factor while still covering the low frequencies well. Indeed, at this acceleration factor (1140 shots), a regular SOS would only have 5 shots per plane while the z-variable-density SOS presents twice as more shots in the center of the k-space. Moreover, a standard GRAPPA-accelerated Cartesian scans was also performed for an iPAT of 4 lasting 14 min 31 s. Results are shown in Fig. 6 for coronal, sagittal, axial planes and a magnified central region of the axial image. Each column corresponds to a different acquisition strategy.

Of all 69-fold accelerated scans, the SPARKLING method presents the best image quality. For instance, the dendritic arborization in the cerebellum in the sagittal slice as well as the magnified region of the axial slice both appear significantly more blurry in 3D radial than in SPARKLING. Regarding the Poisson disk lines

strategy, it is clearly not competitive in this setup as the high acceleration factor translates into a high sub-sampling factor in plane. These visual observations are corroborated by the SSIM scores, calculated for a central axial slice with the iPAT 4 image taken as reference. The SPARKLING image has 0.14 SSIM value larger than the radial, and 0.28 SSIM value better than the Poisson disk strategy.

#### C. High in plane resolution

Finally, images were acquired at a high in plane resolution of 0.3 mm with a slice thickness of 1.5 mm. A standard iPAT 2 PF 6/8 (phase and slice) scan was collected, which is commonly used in the literature of GRE for susceptibility weighted imaging (SWI) at 7 Tesla [27], and is shown in Fig. 7a. SPARKLING-accelerated acquisitions were also performed for an acquisition time of 2 min 43 s and 1 min 24 s as illustrated in Fig. 7b-c. We can observe that the SPARKLING acquisitions yield good image quality although 4 and 10 times faster than the Cartesian scan, respectively.

## VI. DISCUSSION

Among the three studied approaches of 3D SPARKLING (i.e., regular SOS, z-variable-density SOS and fully 3D SPARKLING), we observed that the z-variable-density SOS was the most promising. It allows to perform a variable density along the partition direction, thus allowing to trade high frequency contents for low frequency ones, in contrast to the regular SOS. It thus pushes the undersampling factor even further.

Regarding the performance of the fully 3D SPARKLING which was behind the SOS strategies, one may propose several explanations. First, the constraint to generate the shots *separately* introduces some structure in the sampling, which leads to a degraded global distribution of the samples compared to 2D SPARKLING. To investigate this in detail, it can be useful to look at all the samples of a 3D SPARKLING trajectory present in a plane of thickness one k-space pixel. These plane sections are shown in Fig. 8 for different axes and altitudes. Overall, asymmetric structures can be observed in these plane sections, due to the rotation of one SPARKLING-generated shot to fill one latitude of the k-space. In addition, the distribution of the samples is not

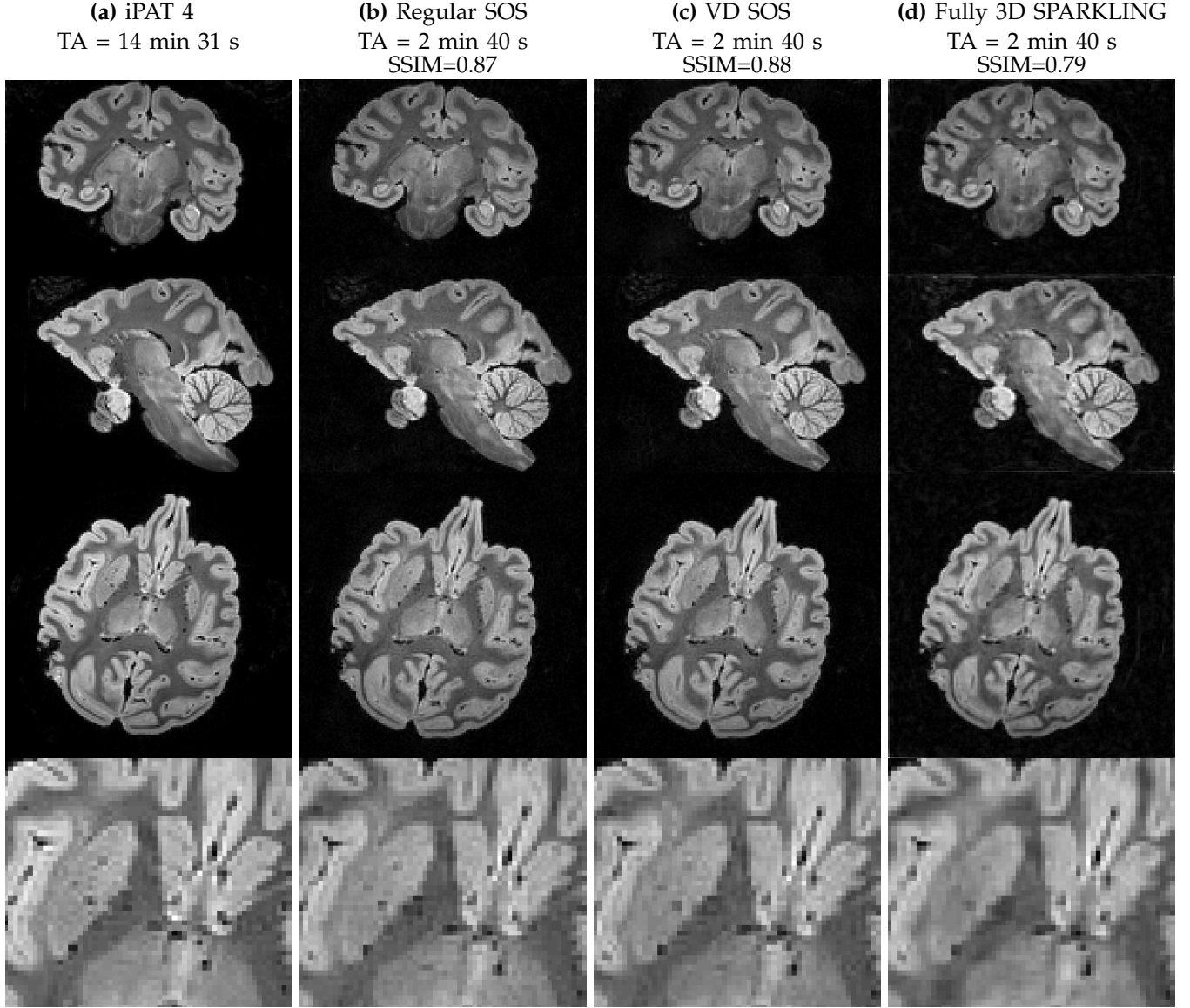


Fig. 5. **600  $\mu\text{m}$  isotropic ex vivo results comparing different SPARKLING strategies.** Column (a): iPAT 4 (GRAPPA) acquisition lasting TA=14min31s. Column (b): regular stack-of-SPARKLING (SOS) results for an acquisition time of TA=2min40s. Column (c): z-variable-density SOS for an acquisition time of TA=2min40s. Column (d): fully 3D SPARKLING for an acquisition time of TA=2min40s. Rows 1 to 4 respectively display a coronal slice, a sagittal slice, an axial slice and a magnified region of the latter axial slice. SSIM scores with the iPAT4 image as reference were computed in an axial slice. FOV was  $200 \times 200 \times 140 \text{ mm}^3$ .

as neat as it was for 2D SPARKLING, in terms of local uniformity for instance. Moreover, the center of the k-space seems to be critical as well: since the samples of different shots are not interacting, the global distribution of the samples in the center is not perfect, with possible under- or oversampling. Hence, the fully 3D SPARKLING approach might be significantly improved by generating all the shots at once. This would however require a considerable development to maintain a reasonable computational time.

In this work, we used the accelerated 3D SPARKLING trajectories to acquire  $T_2^*$ -weighted images of an *ex vivo* baboon brain at a high isotropic resolution of 0.6 mm for a FOV of  $200 \times 200 \times 140 \text{ mm}^3$ . If the iPAT 4 acquisition is considered as a reference scan, the proposed method

allowed to divide the acquisition time by a factor of 20, reducing the scan time from 14 min 31 s to 45 s, while maintaining good image quality. Compared to the fully sampled Cartesian, this acceleration factor would reach 80. For the studied imaging protocol, we also compared the SPARKLING method to other 3D methods such as 3D radial and the Poisson-disk-lines (PD-lines) proposed by Lustig et al., for the same acquisition time of 45 s. The proposed method performed significantly better than these two techniques which both appear blurry, showing the limitations of sampling along lines only. Interestingly, this shows that in 3D, the PD-lines method is not adapted to all imaging scenarios using compressed sensing: it may be interesting for short readouts but for longer readouts applications such as

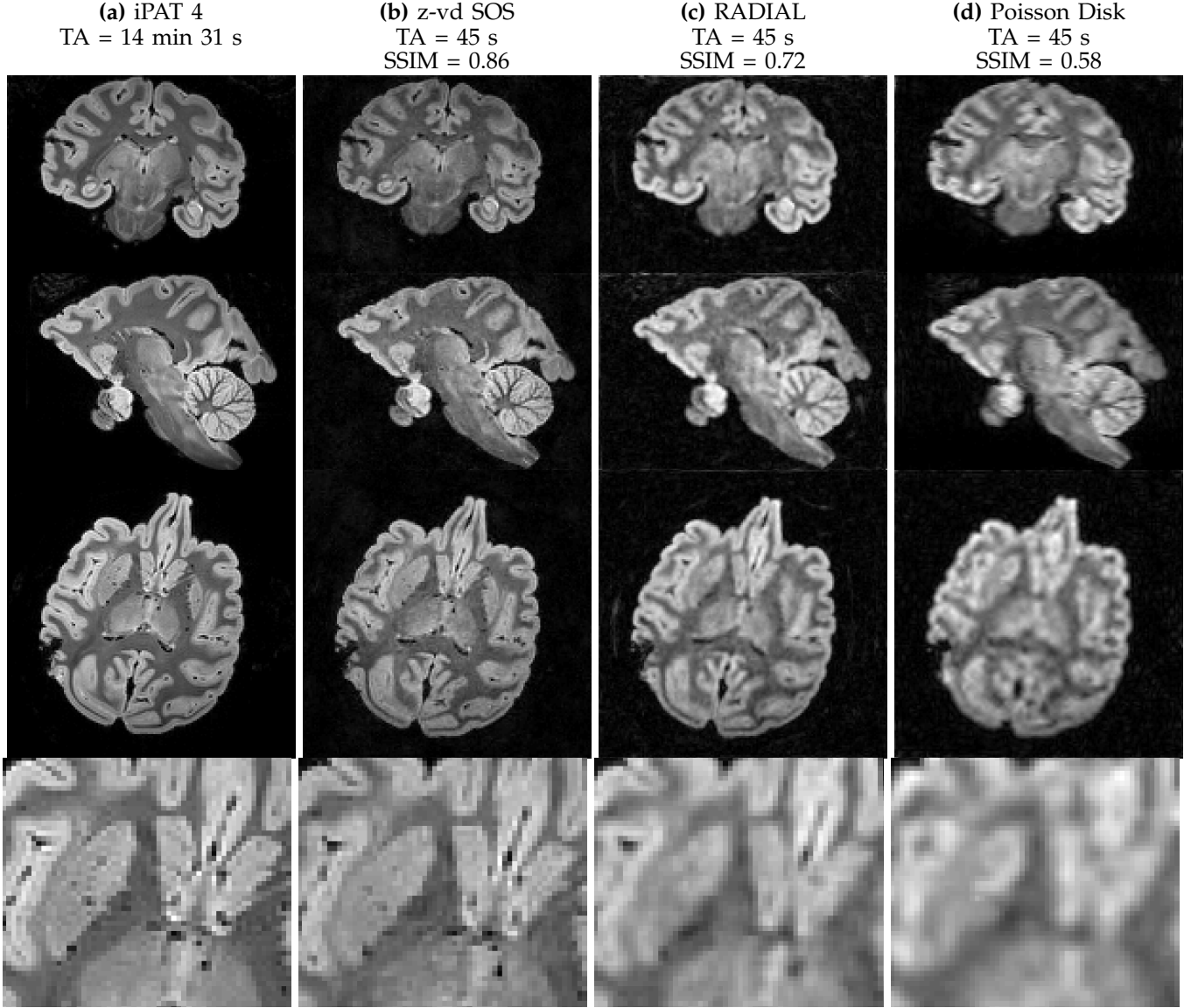


Fig. 6. 0.6 mm isotropic *ex vivo* results comparing z-variable stack-of-sparkling (SOS), 3D radial and 3D Poisson disk lines (PD-lines) sampling for a total number of shots of 1140, i.e., an acquisition time of 45 s. FOV was  $200 \times 200 \times 140 \text{ mm}^3$ .

T2\* weighted imaging (e.g. SWI) it is not as efficient as the SPARKLING approach. Hence, for sufficiently long readouts which allow the SPARKLING trajectories to wiggle significantly, our method leads to better image quality than PD-lines in the framework of compressed sensing. In this regard, the recent waive-CAIPI strategy should perform better than PD-lines and would be an interesting comparison for a further study [33].

For a high in plane resolution of 0.3 mm, a slice thickness of 1.5 mm and a FOV of  $200 \times 200 \times 140 \text{ mm}^3$ , the SPARKLING method was also able to significantly reduce the acquisition time. Compared to the standard sequence used in the context of high resolution SWI (iPAT 2 Partial Fourier 6/8) which lasted 12 min 04 s, the proposed method yielded a similar image quality in only 1 min 24 s. Perhaps, the acceleration could be pushed even further and enable to reduce the acquisition time below one minute while still presenting diagnostic

image quality.

These encouraging *ex vivo* results are yet to be fully validated with *in vivo* acquisitions for which off-resonance effects may be a concern.

## VII. CONCLUSIONS

In this work, we proposed to use the SPARKLING strategy to accelerate the scan time of high resolution T2\*-weighted 3D acquisitions. Among the three studied approaches of 3D SPARKLING, it was observed that a stack-of-SPARKLING with variable density and number of shots along the partition direction was the most promising. Compared to a reference iPAT4 Cartesian scan, the proposed method allowed to divide the acquisition time by a factor of 20, while maintaining good image quality at a 0.6 mm isotropic resolution. Moreover, we compared SPARKLING to other 3D sampling methods such as 3D radial and the Poisson-disk-lines,



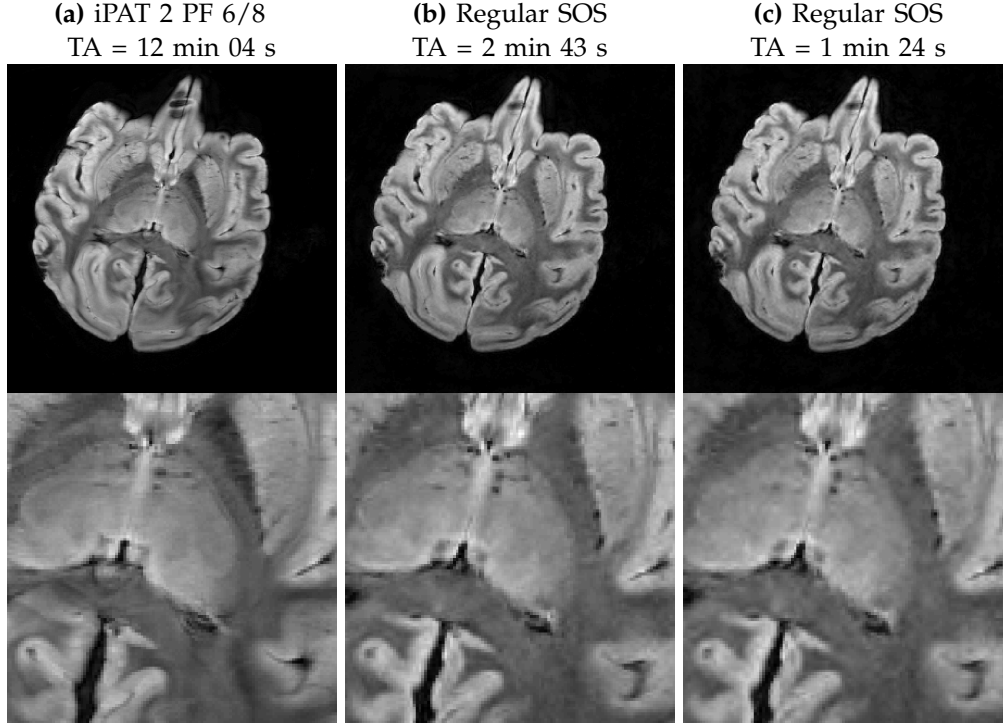


Fig. 7. *Ex vivo* results of high in plane resolution of 0.3 mm and 1.5-mm slice thickness for 96 slices. The reference Cartesian scan used iPAT 2 with partial Fourier 6/8 (phase and slice encode) and lasted 12 min 04 s. The two Regular stack-of-sparkling (SOS) schemes were composed of 2090 shots and 4085 shots, corresponding to acquisition times of 1 min 24 s and 2 min 43 s, respectively. FOV was  $200 \times 200 \times 140 \text{ mm}^3$ .

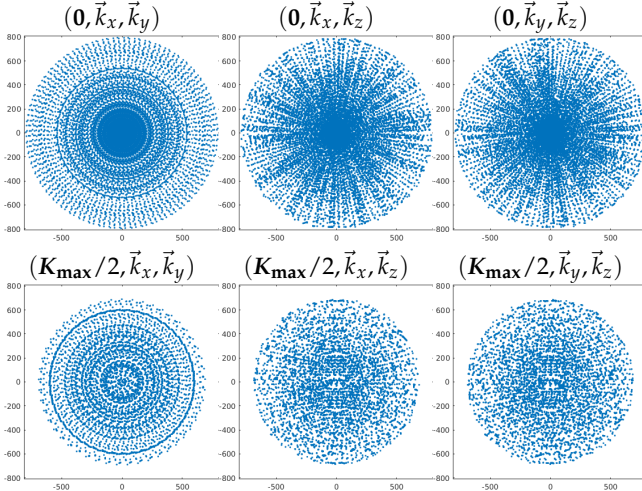


Fig. 8. From left to right: plane sections of an isotropic fully 3D SPARKLING trajectory showing all the samples contained in a plane of thickness one k-space pixel ( $1/\text{FOV}$ ). The plane sections are crossing the origin  $\mathbf{0} = (0, 0, 0)$  (top row) of the k-space or half the maximum spatial frequency  $K_{\max}/2 = (K_{\max}/2, K_{\max}/2, K_{\max}/2)$  (bottom row) for different directions. Because of isotropy, we used the same  $K_{\max}$  over all axes.

for an isotropic resolution of 0.6 mm and a constant acquisition time of 45 s. In the presented *ex vivo* experiments, the proposed method performed significantly better than these two techniques which both appeared blurry. Finally, the 3D SPARKLING method was also used for a very high in plane resolution of 0.3 mm and was shown to maintain a good image quality in just 2 minutes compared to the reference Cartesian scan

of 12 minutes. A straightforward application may be ultrafast 3D susceptibility-weighted imaging [27].

#### ACKNOWLEDGEMENTS

This research program was supported by a 2016 DRF Impulsion grant (COSMIC, P.I.: P.C.). C.L. was also supported by the CEA international PhD program. P.W. was supported by the ANR JCJC OMS. We would like to thank Nicolas Boulant for his insightful remarks. The authors are thankful to Dr Patrick Martigne (Department of Radiobiology, IRBA, Brétigny-sur-Orge, France) for the preparation of the *ex vivo* baboon brain.

#### REFERENCES

- [1] M. Lustig, D. Donoho, and J. M. Pauly, "Sparse MRI: The application of compressed sensing for rapid MR imaging," *Magnetic Resonance in Medicine*, vol. 58, no. 6, pp. 1182–1195, 2007.
- [2] G. Puy, P. Vandergheynst, and Y. Wiaux, "On variable density compressive sampling," *IEEE Signal Processing Letters*, vol. 18, no. 10, pp. 595–598, 2011.
- [3] B. Adcock, A. C. Hansen, C. Poon, and B. Roman, "Breaking the coherence barrier: A new theory for compressed sensing," vol. 5, 2017.
- [4] C. Boyer, J. Bigot, and P. Weiss, "Compressed sensing with structured sparsity and structured acquisition," *Applied and Computational Harmonic Analysis*, 2017.
- [5] P. E. Larson, P. T. Gurney, and D. G. Nishimura, "Anisotropic field-of-views in radial imaging," *IEEE Transactions on Medical Imaging*, vol. 27, no. 1, pp. 47–57, 2008.
- [6] S. S. Vasanawala, M. T. Alley, B. A. Hargreaves, R. A. Barth, J. M. Pauly, and M. Lustig, "Improved pediatric MR imaging with compressed sensing," *Radiology*, vol. 256, no. 2, pp. 607–616, 2010.
- [7] P. Irarrazabal and D. G. Nishimura, "Fast three dimensional magnetic resonance imaging," *Magnetic resonance in medicine*, vol. 33, no. 5, pp. 656–662, 1995.

- [8] F. E. Boada, J. S. Gillen, G. X. Shen, S. Y. Chang, and K. R. Thulborn, "Fast three dimensional sodium imaging," *Magnetic resonance in medicine*, vol. 37, no. 5, pp. 706–715, 1997.
- [9] K. M. Johnson, "Hybrid radial-cones trajectory for accelerated MRI," *Magnetic resonance in medicine*, vol. 77, no. 3, pp. 1068–1081, 2017.
- [10] B. M. Dale, J. S. Lewin, and J. L. Duerk, "Optimal design of k-space trajectories using a multi-objective genetic algorithm," *Magnetic resonance in medicine*, vol. 52, no. 4, pp. 831–841, 2004.
- [11] R. Mir, A. Guesalaga, J. Spiniak, M. Guarini, and P. Irarrazaval, "Fast three-dimensional k-space trajectory design using missile guidance ideas," *Magnetic resonance in medicine*, vol. 52, no. 2, pp. 329–336, 2004.
- [12] C. Kumar Anand, A. Thomas Curtis, and R. Kumar, "Durga: A heuristically-optimized data collection strategy for volumetric magnetic resonance imaging," *Engineering Optimization*, vol. 40, no. 2, pp. 117–136, 2008.
- [13] N. Chauffert, P. Ciuciu, J. Kahn, and P. Weiss, "A projection method on measures sets," *Constructive Approximation*, vol. 45, no. 1, pp. 83–111, 2017.
- [14] C. Boyer, N. Chauffert, P. Ciuciu, J. Kahn, and P. Weiss, "On the generation of sampling schemes for Magnetic Resonance Imaging," *SIAM Journal on Imaging Sciences*, vol. 9, no. 4, pp. 2039–2072, 2016.
- [15] C. Lazarus, P. Weiss, N. Chauffert, F. Mauconduit, L. El Gueddari, C. Destrieux, I. Zemmoura, A. Vignaud, and P. Ciuciu, "SPARKLING: variable-density k-space filling curves for accelerated T2\*-weighted MRI," *Magnetic Resonance in Medicine*, Jan. 2019.
- [16] H. K. Song and L. Dougherty, "Dynamic MRI with projection reconstruction and KWIC processing for simultaneous high spatial and temporal resolution," *Magnetic resonance in medicine*, vol. 52, no. 4, pp. 815–824, 2004.
- [17] W. Lin, J. Guo, M. A. Rosen, and H. K. Song, "Respiratory motion-compensated radial dynamic contrast-enhanced (DCE)-MRI of chest and abdominal lesions," *Magnetic resonance in medicine*, vol. 60, no. 5, pp. 1135–1146, 2008.
- [18] D. R. Thedens, P. Irarrazaval, T. S. Sachs, C. H. Meyer, and D. G. Nishimura, "Fast magnetic resonance coronary angiography with a three-dimensional stack of spirals trajectory," *Magnetic resonance in Medicine*, vol. 41, no. 6, pp. 1170–1179, 1999.
- [19] P. Börner and D. Jensen, "Coronary artery imaging at 0.5 T using segmented 3D echo planar imaging," *Magnetic resonance in medicine*, vol. 34, no. 6, pp. 779–785, 1995.
- [20] L. Kasper, M. Engel, C. Barmet, J. Reber, J. Heinzle, K. E. Stephan, and P. K. Paul, "Rapid 3d blipped spiral fMRI at 7 T," in *Proc. Intl. Soc. Mag. Reson. Med.*, vol. 26, no. 5461, 2018.
- [21] D. Stäb, S. Bollmann, C. Langkammer, K. Bredies, and M. Barth, "Accelerated mapping of magnetic susceptibility using 3D planes-on-a-paddlewheel (POP) EPI at ultra-high field strength," *NMR in Biomedicine*, vol. 30, no. 4, p. e3620, 2017.
- [22] N. Chauffert, P. Weiss, J. Kahn, and P. Ciuciu, "A projection algorithm for gradient waveforms design in Magnetic Resonance Imaging," *IEEE Transactions on Medical Imaging*, vol. 35, no. 9, pp. 2026–2039, Sep. 2016.
- [23] C. Schmaltz, P. Gwosdek, A. Bruhn, and J. Weickert, "Electrostatic halftoning," in *Computer Graphics Forum*, vol. 29, no. 8. Wiley Online Library, 2010, pp. 2313–2327.
- [24] T. Teuber, G. Steidl, P. Gwosdek, C. Schmaltz, and J. Weickert, "Dithering by differences of convex functions," *SIAM Journal on Imaging Sciences*, vol. 4, no. 1, pp. 79–108, 2011.
- [25] P. Leopardi, "A partition of the unit sphere into regions of equal area and small diameter," *Electronic Transactions on Numerical Analysis*, vol. 25, no. 12, pp. 309–327, 2006.
- [26] S. Lloyd, "Least squares quantization in PCM," *IEEE transactions on information theory*, vol. 28, no. 2, pp. 129–137, 1982.
- [27] A. Abosch, E. Yacoub, K. Ugurbil, and N. Harel, "An assessment of current brain targets for deep brain stimulation surgery with susceptibility-weighted imaging at 7 Tesla," *Neurosurgery*, vol. 67, no. 6, pp. 1745–1756, 2010.
- [28] M. A. Schmidt, T. Engelhorn, F. Marxreiter, J. Winkler, S. Lang, S. Kloska, P. Goelitz, and A. Doerfler, "Ultra high-field SWI of the substantia nigra at 7T: reliability and consistency of the swallow-tail sign," *BMC neurology*, vol. 17, no. 1, p. 194, 2017.
- [29] C. Moenninghoff, O. Kraff, S. Maderwald, L. Umutlu, J. M. Theysohn, A. Ringelstein, K. H. Wrede, C. Deuschl, J. Altmeppen, M. E. Ladd *et al.*, "Diffuse axonal injury at ultra-high field MRI," *PLoS One*, vol. 10, no. 3, p. e0122329, 2015.
- [30] L. El Gueddari, C. Lazarus, H. Carrié, A. Vignaud, and P. Ciuciu, "Self-calibrating nonlinear reconstruction algorithms for variable density sampling and parallel reception MRI," in *10th IEEE Sensory Array and Multichannel (SAM) signal processing workshop*, Sheffield, UK, Jul. 2018, pp. 415–419.
- [31] J. Keiner, S. Kunis, and D. Potts, "Using NFFT 3—A Software Library for Various Nonequispaced Fast Fourier Transforms," *ACM Transactions on Mathematical Software (TOMS)*, vol. 36, no. 4, p. 19, 2009.
- [32] J.-M. Lin, "Python non-uniform fast fourier transform (PyNUFFT): An Accelerated Non-Cartesian MRI Package on a Heterogeneous Platform (CPU/GPU)," *Journal of Imaging*, vol. 4, no. 3, p. 51, 2018.
- [33] B. Bilgic, B. A. Gagoski, S. F. Cauley, A. P. Fan, J. R. Polimeni, P. E. Grant, L. L. Wald, and K. Setsompop, "Wave-CAIPI for highly accelerated 3D imaging," *Magnetic resonance in medicine*, vol. 73, no. 6, pp. 2152–2162, 2015.